

Over-the-Air Equalization with Reconfigurable Intelligent Surfaces

Emre Arslan, *Student Member, IEEE*, Ibrahim Yildirim, *Graduate Student Member, IEEE*,
Fatih Kilinc, *Student Member, IEEE*, and Ertugrul Basar, *Senior Member, IEEE*

Abstract—Reconfigurable intelligent surface (RIS)-empowered communications is on the rise and is a promising technology envisioned to aid in 6G and beyond wireless communication networks. RISs can manipulate impinging waves through their electromagnetic elements enabling some sort of a control over the wireless channel. In this paper, the potential of RIS technology is explored to perform equalization over-the-air for frequency-selective channels whereas, equalization is generally conducted at either the transmitter or receiver in conventional communication systems. Specifically, with the aid of an RIS, the frequency-selective channel from the transmitter to the RIS is transformed to a frequency-flat channel through elimination of inter-symbol interference (ISI) components at the receiver. ISI is eliminated by adjusting the phases of impinging signals particularly to maximize the incoming signal of the strongest tap. First, a general end-to-end system model is provided and a continuous to discrete-time signal model is presented. Subsequently, a probabilistic analysis for the elimination of ISI terms is conducted and reinforced with computer simulations. Furthermore, a theoretical error probability analysis is performed along with computer simulations. It is demonstrated that with the proposed method, ISI can successfully be eliminated and the RIS-aided communication channel can be converted from frequency-selective to frequency-flat.

Index Terms—6G, Reconfigurable Intelligent Surface (RIS), Equalization, Frequency-Selective fading, Multipath fading

I. INTRODUCTION

COMMERCIAL fifth generation (5G) wireless network standards have successfully been developed and countries are striving to adapt to 5G as means to not trail behind. Meanwhile, the race for the next generation wireless has already begun as academia and industry advance towards 6G [1]–[3]. The trend for each generation is known where the 'odd' generations (1G, 3G, 5G) have been regarded as evolutions while the even generations (2G, 4G) might be perceived as revolutions for the communication world, therefore, it is the perfect time to envision a revolution with 6G.

Future 6G applications/use-cases demand solutions to combat challenging communication engineering dilemmas. Several of these applications include truly immersive virtual/augmented reality, holographic communication, remote education and much more [4]. These applications require high

reliability, data rates, and security all in conjunction with low-latency. Future wireless networks, particularly at the physical layer, require unique approaches in terms of flexibility, novel waveforms and techniques to satisfy its stringent requirements.

In light of the above mentioned, to tackle some of these 6G demands, there has been a growing interest among the telecommunication community in manipulating and controlling the wireless propagation environment. Reconfigurable intelligent surface (RIS)-empowered communications, is currently a hot topic with the aim of improving signal quality and dynamically reconfiguring the wireless channel [5]–[9]. RISs have emerged as cost-effective solutions to manipulate the propagation environment with their unique and effective functionalities such as controllable reflecting, absorbing, and shifting phases without buffering or processing the incoming signals, hence, they are qualified as passive components [10].

Recently, numerous noteworthy studies have been carried out demonstrating the potential of RIS technologies towards 6G wireless networks. In the literature, RISs have been integrated with existing technologies such as orthogonal frequency division multiplexing (OFDM) and multiple-input multiple-output (MIMO) to enhance their performance. Solutions have been proposed for fast and efficient channel estimation, maximizing the average sum-rate over subcarriers, and maximizing the downlink achievable rate for the user by jointly optimizing the transmit power allocation at the BS and the passive reflection coefficients at the RIS [11]–[17]. The RIS concept has also been investigated to work collectively with related approaches, such as relaying and backscatter communications. Flexible and cost/power effective hybrid transmission schemes involving a relay and a passive RIS are presented in [18]. In addition, fair comparisons have been made between relays and RISs based on SINR maximization for different scenarios such as varying pathloss models and RIS positionings [19]. Furthermore, RIS channel models have been investigated thoroughly for different scenarios such as indoor and outdoor applications and their benefits have been emphasized [20].

In general, RIS literature mostly tends to focus on maximizing the sum-rate/achievable rate of a wireless communication system by adjusting the reflection phases of incoming signals to the RIS, hence, improving the signal-to-noise ratio (SNR) at the target receiver or receivers [21]. However, there have been other captivating studies with different approaches such as investigating the operation of an RIS under predictable mobility considering Doppler effect and delay spread [22], feasibility of mitigating multipath fading and Doppler effects stemming from mobile receivers [23] and so on [24]–[29]. In

E. Arslan, F. Kilinc, and E. Basar are with the Communications Research and Innovation Laboratory (CoreLab), Department of Electrical and Electronics Engineering, Koç University, Sariyer 34450, Istanbul, Turkey. e-mail: earslan18@ku.edu.tr, fkilinc20@ku.edu.tr, ebasar@ku.edu.tr

I. Yildirim is with the Faculty of Electrical and Electronics Engineering, Istanbul Technical University, Istanbul 34469, Turkey. e-mail: yildirimib@itu.edu.tr

general, studies in the literature mostly consider flat-fading systems, and frequency-selective fading is not sufficiently investigated within the context of RIS systems except for some promising OFDM-based RIS solutions. Conventionally, for systems without OFDM, equalization is applied at the receiver (Rx) to combat frequency selectivity; however, it is not always efficient. For example, numerous systems, such as Internet-of-Things (IoT) devices, will be connected wirelessly in the future and it is not efficient for them to implement complex equalization algorithms. Thus, over-the-air equalization with a passive RIS is an efficient alternative for these devices requiring equalization. To the best of the authors' knowledge, existing studies in the literature severely lacks a thorough analysis of equalization methods with the aid of an RIS. Specifically, inter-symbol interference (ISI) caused by multipath fading has been reduced by optimizing the phase shifts at the RIS with the help of an iterative algorithm very recently [30]. Nonetheless, a unified framework for multipath fading mitigation as well as a comprehensive analysis on the potential effects of ISI are still missing in the open literature.

Against this background, this paper analyzes an RIS-aided wireless network and introduces a novel way to equalize the channel over-the-air. In other words, our system transforms the frequency-selective channel between the transmitter (Tx) and the RIS to frequency-flat, resulting in a end-to-end frequency flat channel from the perspective of the receiver. Specifically, the RIS adjusts its phases to eliminate only the phase terms of the first tap of the Tx-RIS propagation channel. Thus, only the magnitude of the strongest tap has been boosted in a clever manner using the RIS while the other non-optimized taps are regarded as ISI terms. In other words, the ISI terms are alleviated by maximizing the first tap of the channel response. We show that when the first tap becomes at least 10 times stronger in terms of squared magnitude, the ISI terms become negligible, hence, reliable transmission will be provided by suppressing the effect of ISI terms. The contributions of this study can be summarized and highlighted as follows:

- A unified framework is proposed to alleviate the frequency-selectivity of the end-to-end system by eliminating the ISI resulting from multipath components.
- A thorough end-to-end system model of the proposed scheme from continuous-time to discrete-time domain is provided and analyzed along with computer simulations.
- The ISI elimination probability is calculated for different configurations using a probabilistic approach.
- A theoretical error probability analysis is provided along with computer simulation results for varying parameters and scenarios.

The rest of the paper can be summarized as follows. In Section II, the generalized end-to-end system model of the proposed scheme is presented. In Section III, an analysis of the probability of ISI elimination is conducted. Section IV provides the error probability analysis of the system and in Section V, computer simulation results are given. Finally, in Section VI the paper is concluded with the final remarks.

II. END-TO-END SYSTEM MODEL

In this section, we consider a linear time-invariant (LTI) and wideband communication system in the presence of an RIS and present our end-to-end system model.

In wideband communication systems, the symbol time T is shorter than the inverse of coherence bandwidth, that is, the delay spread. Since the multipath delay spread is larger than the symbol time, different multipath components interfere with each other. Therefore, in general, the multipath components of this system are resolvable and the difference of the delays between the components significantly exceeds the symbol duration. This interference results in a well known distortion called inter-symbol interference (ISI) which makes the channel frequency-selective. The goal of the proposed system is to eliminate ISI via an RIS and transform the end-to-end frequency-selective channel to frequency-flat, i.e., by accomplishing some sort of virtual equalization over-the-air.

Under the LTI assumption, we can express a general communication system's received continuous-time signal $y(t)$ in the absence of noise using the convolution integral as

$$y(t) = \int_{-\infty}^{\infty} h_c(\tau)x(t - \tau)d\tau \quad (1)$$

where $h_c(t)$ is the end-to-end channel impulse response, $x(t)$ is the transmitted signal, and τ is the delay term. It is possible to transition to discrete-time by sampling the continuous-time signal $y(t)$, and rewriting the communication signal model as

$$y[n] = \sum_{k=-\infty}^{\infty} h[k]x[n - k]. \quad (2)$$

Since the input is band-limited, only the portion of $h_c(t)$ that exists in the bandwidth of $x(t)$ is important to us. By applying an ideal lowpass filter with the same bandwidth as the input signal, we can obtain the continuous-time complex baseband channel as [31]

$$h(t) = B \int \text{sinc}(B(t - \tau))h_c(\tau)e^{j2\pi f_c \tau} d\tau, \quad (3)$$

where B and f_c stand for the complete bandwidth of the ideal lowpass filter and the operating frequency, respectively. As illustrated in Fig. 1, an outdoor and RIS-assisted communication system is considered under the blocked line-of-sight (LOS) path between the Tx and Rx. Here, the channel from the Tx to the RIS is frequency-selective and from the RIS to the Rx is frequency-flat due to the close positioning of the RIS to the Rx, which is a common assumption in the literature due to the multiplicative path-loss of passive RIS systems. The RIS is not placed near the Tx side because even when the RIS equalizes the channel, due to the far distance the signal travels to the Rx, may cause the channel to become frequency selective again. Therefore, the positioning of the RIS being closer to the Rx is preferred allowing a frequency-flat path from the RIS to the Rx. The RIS is equipped with M passive reflecting elements that may be adjusted according to the wireless channel. In baseband, the transmitted signal $x(t)$, with bandwidth $B/2$, is a band-limited signal that is the input to an LTI-type communication system with impulse response

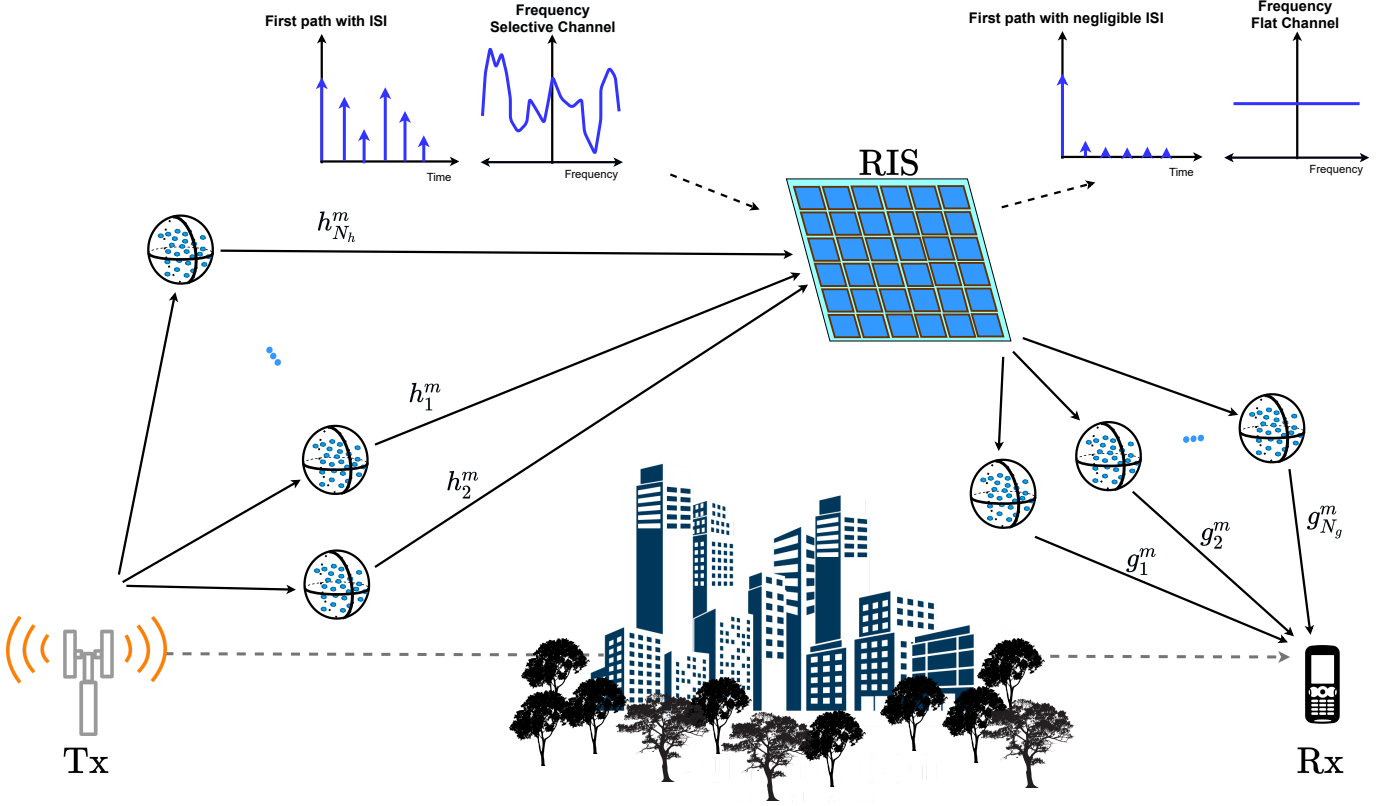


Fig. 1. Proposed over-the-air equalization system model with N_h -paths between Tx-RIS and N_g paths between the RIS-Rx.

$h_c(t)$. In Fig. 1, a general system with N_h paths from the Tx to the RIS and N_g paths from the RIS to the Rx is presented. We assume a frequency-selective channel only between the Tx and the RIS, and a frequency-flat channel between the RIS and Rx in the generic setup of Fig. 1, that is, the N_g multipath components between the RIS and Rx are non-resolvable. The continuous-time impulse response of the end-to-end channel in Fig. 1 can be given as

$$h_c(t) = \sum_{m=1}^M \sum_{l_1=1}^{N_h} \sum_{l_2=1}^{N_g} \alpha_{l_1} \beta_{l_2} \delta(t - \tau_{l_1}^m - \xi_{l_2}^m) e^{j\theta_m}, \quad (4)$$

where α_{l_1} , β_{l_2} , $\tau_{l_1}^m$, $\xi_{l_2}^m$, represent the channel amplitudes and delays of the l_1 th and l_2 th path through the m th RIS element, corresponding to the Tx-RIS and RIS-Rx channels, respectively. Furthermore, $e^{j\theta_m}$ represents the adjustable phase term for the m th RIS element. Since the RIS acts as an LTI filter, $e^{j\theta_m}$ is not dependent on time for one symbol duration.

The continuous-time channel response in (3) can be written in discrete form as follows [31]

$$h[k] = Th(kT), \quad (5)$$

where $T = \frac{1}{B}$. By applying an ideal lowpass filter, with sinc type Nyquist pulse shaping, and the same bandwidth as the input signal similarly from (3), we may simplify (4) to discrete

form by using (5) and obtain

$$h[n] = \int \text{sinc}(n - B\tau) h_c(\tau) e^{-j2\pi f_c \tau} d\tau = \sum_{m=1}^M \sum_{l_1=1}^{N_h} \sum_{l_2=1}^{N_g} \alpha_{l_1} \beta_{l_2} e^{j\theta_m} \times \text{sinc}(n - B(\tau_{l_1} + \xi_{l_2})) e^{-j2\pi f_c (\tau_{l_1} + \xi_{l_2})}. \quad (6)$$

It should be noted that since the delays among the RIS elements are insignificant compared to propagation delays, the $(\cdot)^m$ terms stemming from (4) inside the sinc function in (6) are removed and the delay for the 1st RIS element is used for all RIS elements. In (6), $\tau_{l_1} + \xi_{l_2}$ may be a fraction of a symbol period resulting in an impairment where the receiver does not sample precisely at the right time. Therefore, to counter this impairment, symbol synchronization is employed at the Rx to fix the sample timing error by enabling the delays $\tau_{l_1} + \xi_{l_2}$ become integer fractions of the symbol duration. When symbol synchronization is applied at the receiver, (6) can be re-expressed as follows [31]

$$h[n] = \sum_{m=1}^M \sum_{l_1=1}^{N_h} \sum_{l_2=1}^{N_g} h_{l_1}^m g_{l_2}^m e^{j\theta_m} \delta(n - B\tilde{\tau}_{l_1} - B\tilde{\xi}_{l_2}), \quad (7)$$

where $\tilde{\tau}$ and $\tilde{\xi}$ represent the non-fractional (integer) delays of the paths after symbol synchronization. It is worth noting that the delay terms in the exponential of (6) are now combined

with the channel coefficients for the m^{th} element of each path, which are denoted as

$$\begin{aligned} h_{l_1}^m &= \alpha_{l_1} e^{-j2\pi f_c \tau_{l_1}^m}, \\ g_{l_2}^m &= \beta_{l_2} e^{-j2\pi f_c \xi_{l_2}^m}. \end{aligned} \quad (8)$$

Hereby, the complex baseband received signal $y(t)$ may be written in discrete form as in (2), by sampling at integer multiples of T as $y[n] = y(nT)$. The received signal corrupted with additive white Gaussian noise (AWGN) samples $w[n]$ where $w \sim \mathcal{CN}(0, W_0)$ with $\mathcal{CN}(0, \sigma^2)$ denoting complex Gaussian distribution with variance σ^2 , may be expressed as

$$y[n] = \sum_{m=1}^M \sum_{l_1=1}^{N_h} \sum_{l_2=1}^{N_g} h_{l_1}^m g_{l_2}^m e^{j\theta_m} x[n - B\tilde{\tau}_{l_1} - B\tilde{\xi}_{l_2}] + w[n]. \quad (9)$$

If we arrange the first path term and other terms separately, which will be treated as ISI later on, the received signal can be reorganized as

$$\begin{aligned} y[n] &= \sum_{m=1}^M h_{l_1}^m g_{l_2}^m e^{j\theta_m} x[n - B\tilde{\tau}_1 - B\tilde{\xi}_1] \\ &+ \sum_{m=1}^M \sum_{\substack{l_1=1 \\ (l_1, l_2) \neq (1, 1)}}^{N_h} \sum_{l_2=1}^{N_g} h_{l_1}^m g_{l_2}^m e^{j\theta_m} x[n - B\tilde{\tau}_{l_1} - B\tilde{\xi}_{l_2}] + w[n]. \end{aligned} \quad (10)$$

Even when the symbol timing has been corrected, another impairment occurs with larger delays due to an unknown propagation delay, which is a multiple of the symbol period. These integer offsets create a mismatch between the indices of the transmitted and received symbols, and the correction of this impairment requires frame synchronization [31]. After frame synchronization is applied, the discrete-time received signal in (10) is rewritten as

$$\begin{aligned} y[n] &= \sum_{m=1}^M h_{l_1}^m g_{l_2}^m e^{j\theta_m} x[n] + \sum_{m=1}^M \sum_{\substack{l_1=1 \\ (l_1, l_2) \neq (1, 1)}}^{N_h} \sum_{l_2=1}^{N_g} h_{l_1}^m g_{l_2}^m e^{j\theta_m} \\ &\times x[n - ((B\tilde{\tau}_{l_1} + B\tilde{\xi}_{l_2}) - (B\tilde{\tau}_1 + B\tilde{\xi}_1))] + w[n], \end{aligned} \quad (11)$$

where $h_{l_1}^m g_{l_2}^m = |h_{l_1}^m| |g_{l_2}^m| e^{j\phi_m}$, $h_{l_1}^m g_{l_2}^m = |h_{l_1}^m| |g_{l_2}^m| e^{j\psi_m^{l_1, l_2}}$, and $|\cdot|$ is the absolute value operator. Hence, we may express the signal-to-interference-noise ratio (SINR) γ , of the system as follows:

$$\gamma = \frac{E_s |\sum_{m=1}^M |h_{l_1}^m| |g_{l_2}^m| e^{j\phi_m} e^{j\theta_m}|^2}{E_s |\sum_{m=1}^M \sum_{l_1=1}^{N_h} \sum_{l_2=1}^{N_g} |h_{l_1}^m| |g_{l_2}^m| e^{j\psi_m^{l_1, l_2}} e^{j\theta_m}|^2 + W_0}. \quad (12)$$

Here E_s is the energy of the transmitted signal, $\phi_m = \angle(h_{l_1}^m g_{l_2}^m)$, and $\psi_m^{l_1, l_2} = \angle(h_{l_1}^m g_{l_2}^m)$, where $\angle(\cdot)$ denotes the phase of a complex term. By adjusting the RIS phases according to the first tap as $\theta_m = -\phi_m$, the phase terms of the numerator are eliminated and γ is simplified to

$$\gamma = \frac{E_s (\sum_{m=1}^M |h_{l_1}^m| |g_{l_2}^m|)^2}{E_s |\sum_{m=1}^M \sum_{l_1=1}^{N_h} \sum_{l_2=1}^{N_g} |h_{l_1}^m| |g_{l_2}^m| e^{j\psi_m^{l_1, l_2}} e^{j\theta_m}|^2 + W_0}. \quad (13)$$

Here we aim to arrange $e^{j\theta_m}$ specifically to cancel out the phase terms of the first path ϕ_m , that is, the phase of the numerator. Hence, the numerator of the SINR becomes real valued while the denominator with the ISI components are complex and deteriorated with the additional random phases. In this way, we can maximize the first and strongest tap of the system making it several times more powerful in terms of magnitude than the combined ISI terms, which will be further analyzed in Section III to eliminate the ISI effect.

III. INTER-SYMBOL INTERFERENCE ELIMINATION: A PROBABALISTIC APPROACH

In this section, ISI elimination concept introduced in Section II is analyzed with a detailed probabilistic approach via computer simulation results. For the sake of simplicity, in the rest of this paper, we assume only one path ($N_g = 1$) from the RIS to the Rx unless stated otherwise, since the corresponding channel experiences flat fading due to close positioning of the RIS to the Rx. We remove the underscore and denote the single path from the RIS-Rx simply as g^m . The channel fading coefficients of the Tx-RIS path, $h_{l_1}^m$ where $l_1 = 1, \dots, N_h$ and the single path from the RIS to the Rx, g^m , reflecting from the m^{th} RIS element $m = 1, \dots, M$ are independent and identically distributed under the Rayleigh fading assumption for a worst-case scenario analysis. Hence, these channel coefficients follow the distribution $h_{l_1}^m, g^m \sim \mathcal{CN}(0, \sigma^2)$, where σ^2 is a function of the large scale path loss. We may express the end-to-end channels for the first path and the ISI paths respectively as A and B :

$$\begin{aligned} A &= \sum_{m=1}^M h_{l_1}^m e^{j\theta_m} g^m = \sum_{m=1}^M |h_{l_1}^m| |g^m|, \\ B &= \sum_{m=1}^M \sum_{l_1=2}^{N_h} h_{l_1}^m e^{j\theta_m} g^m, \end{aligned} \quad (14)$$

where $e^{j\theta_m} = e^{-j(\angle h_{l_1}^m + \angle g^m)}$. Since $h_{l_1}^m$ and g^m are independently Rayleigh distributed random variables, the mean and the variance of their product are $E[|h_{l_1}^m| |g^m|] = \frac{\sigma^2 \pi}{4}$ and $\text{VAR}[|h_{l_1}^m| |g^m|] = \sigma^4 (1 - \frac{\pi^2}{16})$, respectively. When the number of RIS elements M is significantly large, from the Central Limit Theorem, A converges to the real Gaussian distribution where $A \sim \mathcal{N}(\frac{M\pi\sigma^2}{4}, M\sigma^4(1 - \frac{\pi^2}{16}))$. On the other hand, since the phase terms exist in the ISI paths, B converges to the complex Gaussian distribution. The mean and variance of the product of the terms in B are calculated as $E[h_{l_1}^m e^{j\theta_m} g^m] = 0$ and $\text{VAR}[h_{l_1}^m e^{j\theta_m} g^m] = M\sigma^4$ resulting in $B \sim \mathcal{CN}(0, M(N_h - 1)\sigma^4)$. As it can be seen from (14), A and B have g^m as a common term; however, they are independent since they are uncorrelated and Gaussian distributed. To find their correlation coefficient, the covariance of A and B is required and since B has zero mean, it may be expressed as

$$E[AB] = E[(\sum_{m=1}^M h_{l_1}^m e^{j\theta_m} g^m)(\sum_{m=1}^M \sum_{l_1=2}^{N_h} h_{l_1}^m e^{j\theta_m} g^m)]. \quad (15)$$

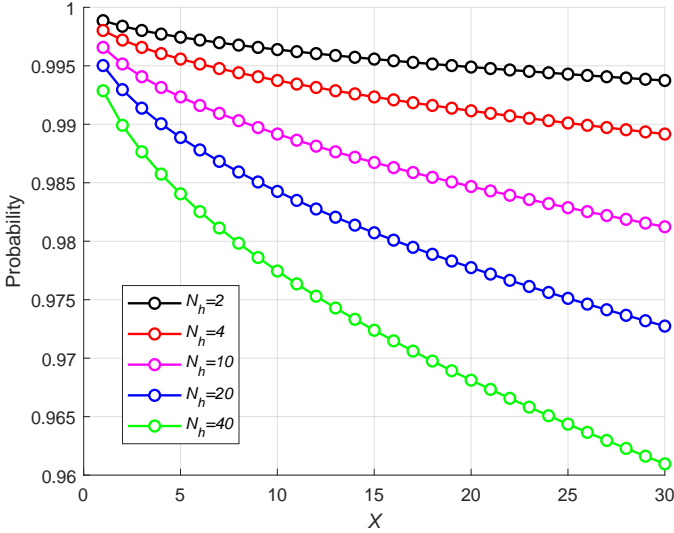


Fig. 2. Probability of RIS-induced first tap channel coefficient being X times greater in squared magnitude than ISI term for $\sigma = 10^{-3}$ and $M = 256$ for varying N_h .

After adjusting the RIS phases according to the first path, (15) may be re-expressed as

$$E[AB] = E\left[\left(\sum_{m=1}^M |h_1^m| |g^m|\right) \left(\sum_{m=1}^M \sum_{l_1=2}^{N_h} h_{l_1}^m e^{-j\angle h_{l_1}} |g^m|\right)\right]. \quad (16)$$

Here, h_{l_1} is a complex Gaussian term with zero mean hence, the covariance is zero. Therefore, the correlation coefficient is also zero resulting in A and B being considered uncorrelated and because they are Gaussian distributed, they are also independent. We assume that when A is at least 10 times greater in squared magnitude than the ISI term B , the ISI term will be negligible and can be ignored. To generalize this, the probability that A is X times greater in squared magnitude than B may be expressed as follows:

$$P(A^2 - X|B|^2 > 0) = 1 - P(C < 0) = 1 - \int_{-\infty}^0 f_C(c) dc, \quad (17)$$

where $C = A^2 - X|B|^2$, and $f_C(c)$ is the probability density function (PDF) of C . Therefore, to ensure successful ISI elimination, we assume that X would be at least 10. In (17), A^2 and $|B|^2$ follow non-central chi-square distribution with one degree of freedom and central chi-square distribution with two degrees of freedom, respectively. Here, C is the difference of independent non-central and central chi-squared random variables [32]. Thus, we integrate the PDF of the difference of non-central chi-squared and central chi-squared random variables accordingly where $P(C < 0)$ is expressed as

$$P(C < 0) = \frac{1}{2\sigma_2^2} \sqrt{\frac{\sigma_2^2}{\sigma_1^2 + \sigma_2^2}} \exp\left(\frac{c}{2\sigma_2^2}\right) \exp\left(\frac{-\mu_1^2}{2(\sigma_1^2 + \sigma_2^2)}\right), \quad (18)$$

where $\mu_1 = M\sigma^2 \frac{\pi}{4}$, $\sigma_1^2 = M\sigma^2(1 - \frac{\pi^2}{16})$, and $\sigma_2^2 = XM(N_h - 1)\sigma^4/2$ stand for the mean and variance of A , and variance of B , respectively. Since M is directly multiplied with a power of σ , for a small σ in practical scenarios, the number of RIS elements M is not expected to effect the result. Substituting

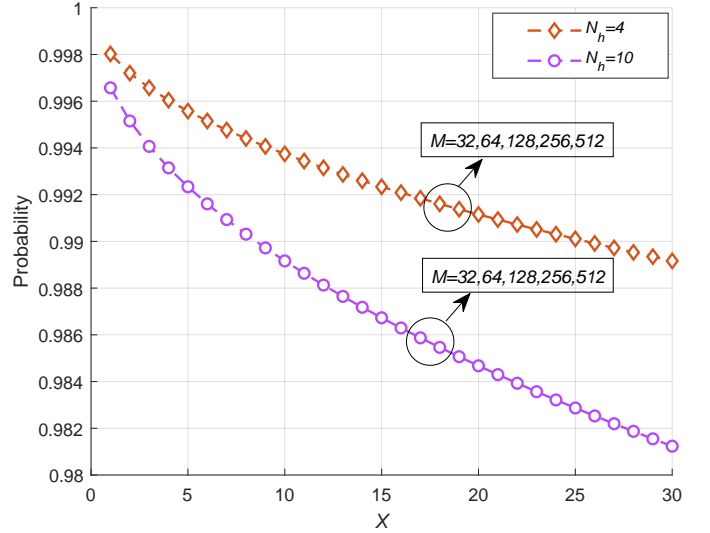


Fig. 3. Probability of RIS-induced first tap being X times greater in squared magnitude than ISI term for $\sigma = 10^{-3}$, $N_h = 4$ and 10 for varying M .

(18) into (17), $P(A^2 - X|B|^2 > 0)$ may be simplified as follows

$$1 - P(C < 0) = 1 - \sqrt{\frac{\sigma_2^2}{\sigma_1^2 + \sigma_2^2}} \exp\left(\frac{-\mu_1^2}{2(\sigma_1^2 + \sigma_2^2)}\right). \quad (19)$$

Computer simulation results in this section provide a clear visualization of the probability of the strongest path being X times greater in squared magnitude than the combined ISI paths allowing us to clearly express that they are negligible and eliminated.

In Fig. 2, we provide the ISI elimination probability in (17) for $N_h = 10$, $M = 256$ and $\sigma = 10^{-3}$. It can be seen that under the worst-case scenario with a uniform power-delay-profile (PDP) and Rayleigh distribution, the probability of the first path being at least $X = 10$ times greater in squared magnitude than the ISI paths is about 99% even for 9 taps causing ISI. In general, Fig. 2 demonstrates that for varying total number of N_h paths, i.e., $N_h - 1$ ISI paths, the probability that the first tap is 10 times greater in squared magnitude than the combined ISI terms is greater than 97.5% even when $N_h = 40$. It can also be seen that not only is it 10 times greater, the first tap is more than 30 times greater in squared magnitude than the combined ISI paths for more than 96% of the time even for $N_h = 40$. Even though the ISI is almost completely negligible, we can see that as the number of ISI terms increases, the probability of the ISI elimination slowly degrades. However, the probability is over 96% for even a large number of ISI paths.

In Fig. 3, N_h is set to 4 and 10 to examine the performance for varying M values (RIS sizes). It can be seen that for a small σ the probability of ISI elimination is unchanged with the RIS size, because as M increases, the results stay the same and the curves fully overlap each other for both cases of N_h . This goes for any RIS size and number of paths. As mentioned previously, this is because in (18), M is multiplied with σ^2 thus, for a small σ , the effect of M in the probability

of elimination is greatly reduced. On the other hand, if σ were to be a large value which is not practical, a change in M would impact the results and the curves in Fig. 3 would not overlap. In addition, it can also be seen that the probability that the first tap is 10 and 30 times greater squared magnitude than the combined ISI terms is over 98% for both cases.

It should be noted that for all computer simulations, we assume a uniform PDP, unless stated otherwise, which models a worst-case scenario, hence, for other PDPs the results would be superior. Additionally, for a smaller σ , the probability of negligible ISI approaches even closer to unity. We can conclude that even in the worst-case scenario, we can eliminate the ISI and maximize the first tap's squared magnitude. These probabilities remain outstanding and ensure that the ISI is almost negligible, which will be further verified in terms of error probability analysis in the next section.

IV. THEORETICAL ERROR PROBABILITY ANALYSIS

In this section, the system of Fig. 1 is revisited, where the transmission is carried out via an RIS under a blocked link between the Tx and Rx. For this setup, $d_{\text{Tx-Rx}}$, $d_{\text{Tx-RIS}}$, $d_{\text{RIS-Rx}}$, represent the distances between the Tx and Rx, Tx and RIS, RIS and Rx, respectively. In addition, h_{Tx} , h_{RIS} , h_{Rx} , and f_c , represent the height of the Tx, RIS, Rx, and the operating frequency, respectively. The 3GPP UMi point-to-point NLOS path loss model for a single Tx/Rx path is also considered [33]. Within the 2–6 GHz frequency band and Tx-Rx distance ranging from 10 – 2000 m, the 3GPP UMi path loss model for NLOS transmission is expressed as:

$$L(d)[\text{dB}] = 36.7\log_{10}(d) + 22.7 + 26\log_{10}(f_c). \quad (20)$$

The fading channel between the single antenna Tx and the m^{th} RIS element, and m^{th} RIS element to the single antenna Rx are denoted as $h_{l_1}^m$ and g^m , respectively. It is assumed that Rayleigh fading channels $h_{l_1}^m$ and g^m follow $\mathcal{CN}(0, \sigma^2)$ distribution where σ^2 is the variance of the complex Gaussian distribution. The RIS is composed of M passive and controllable reflecting elements. Revisiting Section III, the received signal can be written as

$$y[n] = \sum_{m=1}^M \alpha_1^m \beta_1^m e^{j\theta_m} x[n] + \sum_{m=1}^M \sum_{\substack{l_1=1 \\ (l_1, l_2) \neq (1, 1)}}^{N_h} \sum_{l_2=1}^{N_g} \alpha_{l_1}^m \beta_{l_2}^m e^{j\theta_m} \times x[n - ((B\tilde{\tau}_{l_1} + B\tilde{\xi}_{l_2}) - (B\tilde{\tau}_{l_1} + B\tilde{\xi}_{l_2}))] + w[n], \quad (21)$$

where $e^{j\theta_m}$ is the adjustable phase shift introduced by the m^{th} RIS element, $x[n]$ stands for the data symbol selected from Q -ary phase shift keying/quadrature amplitude modulation (PSK/QAM) constellations, and $w \sim \mathcal{CN}(0, W_0)$ is the AWGN term. With the assumption of knowledge of the channel phases at the RIS, it can be seen that by adjusting the θ_m term at the RIS, that is, $\theta_m = -\phi_m$ for $m = 1, \dots, M$, the SINR can be maximized since the channel phases of the first tap is eliminated. Additionally, we assume that the ISI becomes negligible when the first tap is 10 times greater in

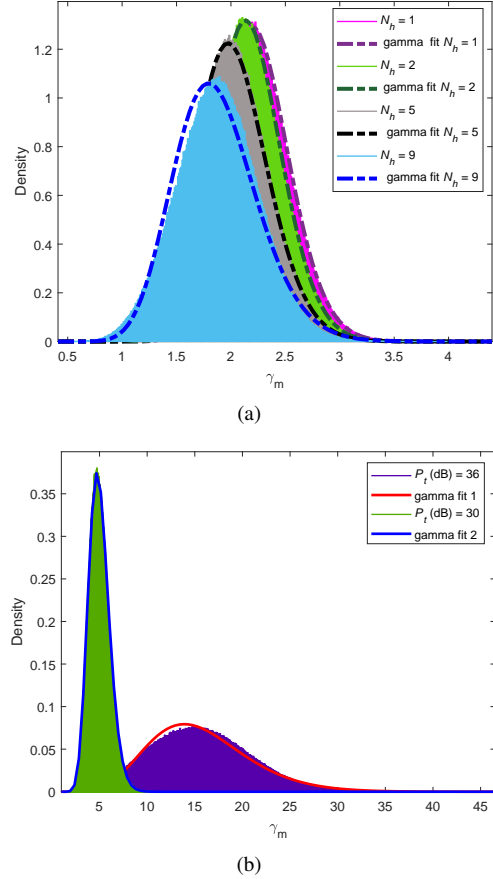


Fig. 4. (a) Density distribution of γ_m for varying N_h and (b) gamma distribution fit for varying P_t .

squared magnitude than the ISI paths. Substituting (14) into (13) the maximized SINR (γ_m) can be approximated as:

$$\gamma_m = \frac{E_s A^2}{E_s |B|^2 + W_0}. \quad (22)$$

Since A^2 is a non-central chi-squared RV with one degree of freedom and $|B|^2$ is central chi-squared, their SINR ratio γ_m cannot be exactly derived and to the best of the authors' knowledge, its closed form has not been reported in the open literature. Thus, a semi-analytical approach is conducted where the distribution of γ_m is generated via MATLAB using dfittool by carefully considering A and B terms.

As we may recall, A^2 is a chi-squared distributed random variable which is a specific case of the gamma distribution. Since the effect of the ISI term $|B|^2$ in γ_m is negligible, we expect γ_m to fit the gamma distribution. Fig. 4(a) shows the PDF of γ_m and its fit to the gamma distribution for varying number of ISI terms ($N_h - 1$) with a fixed RIS size of $M = 128$ and $P_t = 20$ dB. Using the dfittool in MATLAB, it can be confirmed that the distribution of γ_m fits the gamma distribution. As the number of ISI terms are increased, the PDFs of the distributions begin to differ from one another and for a large number of N_h , as seen from the case of $N_h = 9$, the ISI terms start to show an effect and begin to slightly deviate from an exact fit to the gamma distribution. For different parameters such as M , N_h , P_t , W_0 , the gamma

TABLE I
FITTED GAMMA DISTRIBUTION PARAMETERS FOR VARYING P_t AND ISI TERMS

# of Taps	P_t (dB):	0	5	10	15	20	25	30
$N_h = 1$	κ	51.6562	51.7005	51.4739	51.8451	51.7974	51.5856	51.7708
	ρ	0.00043326	0.0013687	0.0043469	0.013647	0.043217	0.13717	0.43220
$N_h = 2$	κ	51.7225	51.7359	51.9001	51.8399	51.0725	41.9911	19.6178
	ρ	0.00043245	0.0013665	0.0042996	0.013529	0.042627	0.15552	0.92227
$N_h = 5$	κ	51.6683	51.9701	51.8661	50.2720	37.5954	15.7829	5.3166
	ρ	0.00043227	0.0013567	0.0042659	0.013598	0.053927	0.34749	2.40733
$N_h = 9$	κ	51.9844	51.8750	51.1083	45.0914	23.9158	8.1000	3.0660
	ρ	0.000429356	0.00135427	0.00428272	0.0147048	0.0783354	0.575313	3.19979

distribution parameters vary and a general expression cannot be derived to express the gamma distribution parameters for given specifications. On the other hand, Fig. 4(b) shows the PDF for $M = 64$ for $P_t = 30$ dB and $P_t = 36$ dB. It can be seen that for $P_t = 30$ dB, the gamma distribution fits perfectly; however for a higher SINR where $P_t = 36$ dB, the gamma distribution does not fit perfectly. This is because as the SINR increases, the effect of the noise diminishes and the ISI term $|B|^2$ starts to become more effective. Thus, the distribution is affected and deviated from the chi-squared distribution, which is a form of the gamma distribution.

To be used in theoretical derivations, for each configuration, the shape κ and scale ρ parameters for the gamma distribution need to be generated. Table I provides the gamma distribution parameters required to calculate the moment generating function (MGF) for different scenarios. Specifically, the gamma distribution has the following MGF

$$M_{\gamma_m}(s) \approx (1 - \rho s)^{-\kappa}, \text{ for } s < \frac{1}{\rho} \quad (23)$$

From (23), we can obtain the average SEP for Q -PSK signaling as in [20],

$$P_e \approx \frac{1}{\pi} \int_0^{(Q-1)\pi/Q} M_{\gamma} \left(\frac{-\sin^2(\pi/Q)}{\sin^2 \eta} \right) d\eta, \quad (24)$$

which for binary PSK (BPSK) simplifies to

$$P_e \approx \frac{1}{\pi} \int_0^{\pi/2} \left(1 + \frac{\rho}{\sin^2 \eta} \right)^{-\kappa} d\eta. \quad (25)$$

V. SIMULATION RESULTS

In this section, computer simulation results for the proposed over-the-air equalization system with an RIS are presented. First, the bit-error rate (BER) of the system is evaluated and compared to theoretical results for varying M and discussed in detail. Subsequently, the BER performance for discrete phases and ideal phases are assessed. Finally, a comparison of the proposed intelligent reflection and plain reflection, where the ISI terms remain, is presented for increasing RIS element size M .

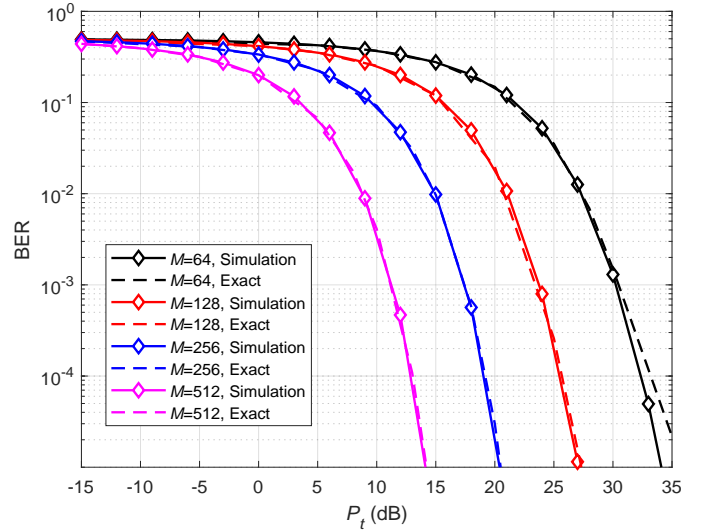


Fig. 5. Comparison of exact and simulated results for varying number of RIS elements M .

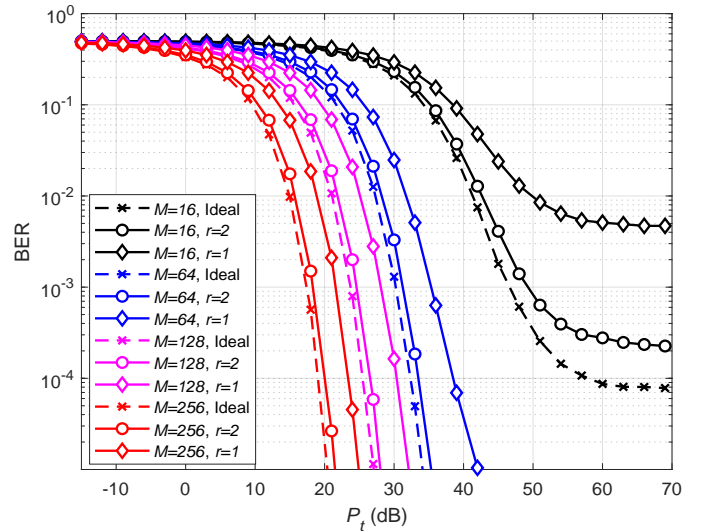


Fig. 6. Performance of discrete phase compared to ideal phase for varying M .

For all computer simulations, path loss is included and the simulation parameters in Table II are used. For the BER analyses, the noise power is fixed to -130 dBm and the

TABLE II
COMPUTER SIMULATION PARAMETERS

Parameter	Value
f_c [GHz]	5
$d_{\text{Tx-Rx}}$ [m]	55.73
$d_{\text{Tx-RIS}}$ [m]	35.51
$d_{\text{RIS-Rx}}$ [m]	20.22
h_{Tx} [m]	10
h_{RIS} [m]	4
h_{Rx} [m]	1
W_0 [dBm]	-130

transmit power P_t is varied.

In Figs. 5 and 6, we present the BER results to verify the effectiveness of ISI elimination for varying N_h and M . It is clear that as the number of RIS elements M increases, the performance significantly increases and less P_t is needed to achieve the same error performance. However, there is a trade-off between cost and performance as M increases. Specifically, from Fig. 5, it can be confirmed that the ISI is negligible as verified by (17). At high BER values and M , computer simulation results exactly match the theoretical curves and confirm the elimination of ISI. As seen from the the case of $M = 64$ at high P_t values, where the noise effect is negligible, the exact BER curves slightly differ than the simulated BER curves and this is because the negligible ISI terms beginning to present themselves which affects the distribution of γ_m as discussed in the previous section. However, for a greater M , even at low BER values, the ISI is nowhere to be seen because as M increases, the effect of the first tap becomes more significant. In other words, the ISI elimination probability is the same for all M as we recall from Fig. 3, however, as M increases in the BER results, the effect of the numerator in (22) becomes more dominant than the remaining ISI terms in the denominator thus, diminishing its effect even more.

Fig. 6 compares the BER performances for ideal and discrete phase adjustments, where r is the bit resolution of the discrete phase levels. For ideal phase adjustments, the phase term at the RIS is set exactly to eliminate the phase of the channel of the first tap. On the other hand, for discrete phase adjustments, the phase shifts at the RIS can only take certain values according to r and it rounded to the closest phase term to maximize the first tap. For example, when $r = 2$, there are $2^r = 4$ possible phases to choose from to maximize the first tap. Since discrete phases may not completely align the phase terms of the first tap, the full potential of the first tap maximization and ISI elimination cannot be achieved. However, if the RIS is large enough, even 1 bit phases, $r = 1$, are enough to boost the desired signal terms. As it can be seen, the discrete case performs noticeably worse compared to the ideal case. For a large M , we do not observe an error floor, on the other hand, for a small number of RIS elements, such as $M = 16$, ISI elimination is not sufficient and an irreducible error floor is observed due to the discrete phases. As the resolution is decreased from 2 to 1, the error floor increases drastically.

Fig. 7 compares the SINR of the proposed over-the-air equalization scheme with a blind reflection from the RIS with no ISI elimination for varying M under uniform and

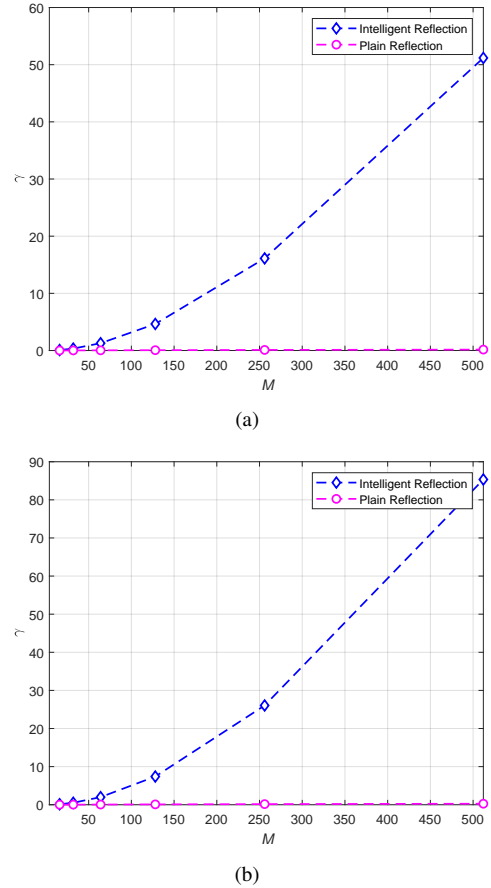


Fig. 7. (a) SINR comparison of the intelligent reflection and non-intelligent reflection for varying M and (a) an uniform PDP (b) an exponential PDP.

exponential PDPs, respectively. Fig. 7(a) presents the performance improvement considering uniform PDP for the worst-case scenario. On the other hand, Fig. 7(b) considers a more realistic exponential PDP. Comparing Figs. 7(a) and 7(b), it can be observed that the more realistic case, an exponential PDP, outperforms the worst-case uniform PDP scenario in terms of ISI minimization. This is because more power is allocated to the first tap in the exponential PDP case hence, exponentially reducing the power of the remaining ISI taps resulting in an increased SINR. When revisiting the BER curves and examining Fig. 7 together, they complement each other where as M increases, the SINR also exponentially increases thus, improving the BER.

VI. CONCLUSION

The main motivation of this study has been to provide a unique approach and perspective to RIS-based systems and simple equalization for frequency-selective channels. It has been shown that an efficient over-the-air equalization concept, independent from the Tx and Rx, can be realized by utilizing the RIS. The RIS adjusts the phases of its elements according to the incoming signals to maximize the magnitude of the first tap, making the ISI terms negligible, hence, maximizing the SINR performance. A complete end-to-end system model and a probabilistic analysis of ISI elimination have been provided. In addition, a theoretical error probability analysis

in conjunction with computer simulation results have shown the advantages of the proposed scheme. Future works may include an extension of this model to different scenarios, such as when a LOS link exists between the Tx and Rx. Also, in the future this model may be analyzed under different channel fading distributions, multiple RISs and for mobile nodes.

REFERENCES

- [1] W. Saad, M. Bennis, and M. Chen, "A vision of 6G wireless systems: Applications, trends, technologies, and open research problems," *IEEE Netw.*, vol. 34, no. 3, pp. 134–142, Oct. 2020.
- [2] J. Zhu, M. Zhao, S. Zhang, and W. Zhou, "Exploring the road to 6G: ABC — foundation for intelligent mobile networks," *China Commun.*, vol. 17, no. 6, pp. 51–67, Jun. 2020.
- [3] C. Yizhan, W. Zhong, H. Da, and L. Ruosen, "6G is coming : Discussion on key candidate technologies and application scenarios," in *Proc. 2020 Int. Conf. on Comput. Commun. and Netw. Security (CCNS)*, Aug. 2020, pp. 59–62.
- [4] S. Doğan-Tusha, H. Arslan *et al.*, "6G vision: An ultra-flexible perspective," *arXiv preprint arXiv:2009.07597*, Sep. 2020.
- [5] Q. Wu and R. Zhang, "Towards smart and reconfigurable environment: Intelligent reflecting surface aided wireless network," *IEEE Commun. Mag.*, vol. 58, no. 1, pp. 106–112, Nov. 2020.
- [6] M. A. El-Mossallamy, H. Zhang, L. Song, K. G. Seddik, Z. Han, and G. Y. Li, "Reconfigurable intelligent surfaces for wireless communications: Principles, challenges, and opportunities," *IEEE Trans. Cogn. Commun. Netw.*, vol. 6, no. 3, pp. 990–1002, May 2020.
- [7] E. Basar and I. Yildirim, "Reconfigurable intelligent surfaces for future wireless networks: A channel modeling perspective," *IEEE Wireless Commun. (to appear)*, Apr. 2021.
- [8] H. Gacanin and M. Di Renzo, "Wireless 2.0: Toward an intelligent radio environment empowered by reconfigurable meta-surfaces and artificial intelligence," *IEEE Veh. Technol. Mag.*, vol. 15, no. 4, pp. 74–82, Sep. 2020.
- [9] S. Alfattani, W. Jaafar, Y. Hmamouche, H. Yanikomeroglu, A. Yon-gacoglu, N. D. Dao, and P. Zhu, "Aerial platforms with reconfigurable smart surfaces for 5G and beyond," *IEEE Commun. Mag.*, vol. 59, no. 1, pp. 96–102, Feb. 2021.
- [10] E. Basar, "Transmission through large intelligent surfaces: A new frontier in wireless communications," in *Proc. 2019 European Conf. Netw. and Commun. (EuCNC)*. IEEE, Jun. 2019, pp. 112–117.
- [11] Y. Yang, S. Zhang, and R. Zhang, "IRS-enhanced OFDM: Power allocation and passive array optimization," in *Proc. 2019 IEEE Global Commun. Conf. (GLOBECOM)*. IEEE, Dec. 2019, pp. 1–6.
- [12] B. Zheng and R. Zhang, "Intelligent reflecting surface-enhanced OFDM: Channel estimation and reflection optimization," *IEEE Wireless Commun. Lett.*, vol. 9, no. 4, pp. 518–522, Dec. 2020.
- [13] Y. Yang, B. Zheng, S. Zhang, and R. Zhang, "Intelligent reflecting surface meets OFDM: Protocol design and rate maximization," *IEEE Trans. Commun.*, vol. 68, no. 7, pp. 4522–4535, Mar. 2020.
- [14] Y. Yang, S. Zhang, and R. Zhang, "IRS-enhanced OFDMA: Joint resource allocation and passive beamforming optimization," *IEEE Wireless Commun. Lett.*, vol. 9, no. 6, pp. 760–764, Jan. 2020.
- [15] H. Li, W. Cai, Y. Liu, M. Li, Q. Liu, and Q. Wu, "Intelligent reflecting surface enhanced wideband MIMO-OFDM communications: From practical model to reflection optimization," *IEEE Trans. Commun.*, pp. 1–1, Mar. 2021.
- [16] S. Lin, B. Zheng, G. C. Alexandropoulos, M. Wen, F. Chen, and S. Mumtaz, "Adaptive transmission for reconfigurable intelligent surface-assisted OFDM wireless communications," *IEEE J. Sel. Areas Commun.*, vol. 38, no. 11, pp. 2653–2665, Jul. 2020.
- [17] B. Zheng, C. You, and R. Zhang, "Fast channel estimation for IRS-assisted OFDM," *IEEE Wireless Commun. Lett.*, Nov. 2020.
- [18] I. Yildirim, F. Kilinc, E. Basar, and G. C. Alexandropoulos, "Hybrid RIS-empowered reflection and decode-and-forward relaying for coverage extension," *IEEE Commun. Lett.*, May 2021.
- [19] J. Ye, A. Kammoun, and M.-S. Alouini, "Spatially-distributed RISs vs relay-assisted systems: A fair comparison," *IEEE Open J. Commun. Soc.*, Feb. 2021.
- [20] I. Yildirim, A. Uyrus, and E. Basar, "Modeling and analysis of reconfigurable intelligent surfaces for indoor and outdoor applications in future wireless networks," *IEEE Trans. Commun.*, Nov. 2020.
- [21] Q. Wu, S. Zhang, B. Zheng, C. You, and R. Zhang, "Intelligent reflecting surface aided wireless communications: A tutorial," *IEEE Trans. Commun. (to appear)*, Jan. 2021.
- [22] B. Matthiesen, E. Björnson, E. De Carvalho, and P. Popovski, "Intelligent reflecting surface operation under predictable receiver mobility: A continuous time propagation model," *IEEE Wireless Commun. Lett.*, Sep. 2020.
- [23] E. Basar, "Reconfigurable intelligent surfaces for Doppler effect and multipath fading mitigation," *Frontiers in Commun. and Netw. (to appear)*, Apr. 2021.
- [24] C. Huang, G. C. Alexandropoulos, C. Yuen, and M. Debbah, "Indoor signal focusing with deep learning designed reconfigurable intelligent surfaces," in *Proc. 2019 IEEE 20th Int. Workshop Sig. Process. Advances in Wireless Commun. (SPAWC)*, Jul. 2019, pp. 1–5.
- [25] T. Hou, Y. Liu, Z. Song, X. Sun, Y. Chen, and L. Hanzo, "Reconfigurable intelligent surface aided NOMA networks," *IEEE J. Sel. Areas Commun.*, vol. 38, no. 11, pp. 2575–2588, Jul. 2020.
- [26] H. Zhang, B. Di, L. Song, and Z. Han, "Reconfigurable intelligent surfaces assisted communications with limited phase shifts: How many phase shifts are enough?" *IEEE Trans. Veh. Technol.*, vol. 69, no. 4, pp. 4498–4502, Feb. 2020.
- [27] S. Hong, C. Pan, H. Ren, K. Wang, and A. Nallanathan, "Artificial-noise-aided secure MIMO wireless communications via intelligent reflecting surface," *IEEE Trans. Commun.*, vol. 68, no. 12, pp. 7851–7866, Sep. 2020.
- [28] S. Li, B. Duo, X. Yuan, Y.-C. Liang, and M. Di Renzo, "Reconfigurable intelligent surface assisted UAV communication: Joint trajectory design and passive beamforming," *IEEE Wireless Commun. Lett.*, vol. 9, no. 5, pp. 716–720, Jan. 2020.
- [29] E. Basar, "Reconfigurable intelligent surface-based index modulation: A new beyond MIMO paradigm for 6G," *IEEE Trans. Commun.*, vol. 68, no. 5, pp. 3187–3196, Feb. 2020.
- [30] H. Zhang, L. Song, Z. Han, and H. V. Poor, "Spatial equalization before reception: Reconfigurable intelligent surfaces for multi-path mitigation," *arXiv preprint arXiv:2103.04784*, Mar. 2021.
- [31] R. W. Heath Jr, *Introduction to Wireless Digital Communication: A Signal Processing Perspective*. Prentice Hall, Apr. 2017.
- [32] M. K. Simon, *Probability distributions involving Gaussian random variables: A handbook for engineers and scientists*. Springer Science & Business Media, May 2007.
- [33] "3rd Generation Partnership Project; Technical specification group radio access network; evolved universal terrestrial radio access (E-UTRA); further advancements for E-UTRA physical layer aspects (release 9)."